Microsystem Technologies
https://doi.org/10.1007/s00542-024-05616-z

TECHNICAL PAPER

Electret vibration energy harvesters with symmetrically configured curved-beam hinges

Dooyoung Hah[1]

Received: 1 August 2023 / Accepted: 31 January 2024

Abstract
For vibration energy harvesters, broadband power spectral characteristics are often desirable. One way of achieving broadband spectrum is to employ curved-beam hinges, utilizing their nonlinear spring characteristics. In our previous study, electret-based vibration energy harvesters employing curved-beam hinges were investigated via numerical analysis based on stochastic differential equations and colored-noise inputs. It showed that the harvesters with curved-beam hinges can produce higher power than the ones with ordinary straight beams when the external acceleration is between $0.02g$ and $0.05g$. It was also learned that the straight-beam device, a Duffing oscillator, performs better than the curved-beam device, a Duffing–Holmes oscillator, at higher acceleration ($\geq 0.1g$). Since the energy harvesting efficiency is one of the most important performance indicators, continuous search for novel configurations with improved efficiency is needed. For that purpose, a symmetric configuration of curved-beam hinges (a Duffing oscillator) is proposed in this work, in contrast to the previously reported one with an asymmetric configuration (a Duffing–Holmes oscillator). This study shows, via numerical analysis, that the symmetric configuration can produce higher (up to 7.3% more) power outputs for the external acceleration magnitude higher than $0.1g$, when compared to an asymmetric configuration. The study results also show that it can produce higher power outputs (up to 4.5 times) than the harvesters employing ordinary straight-beam hinges.

1 Introduction

Mechanical vibrations are present everywhere, and most of them are wasted, without being utilized. Vibration energy harvesters (VEHs) collect those unused vibrations and transform them into a form that can be either used right away or stored for later use. Numerous reports have been made on the topic of VEHs in various aspects, including energy conversion mechanisms, geometry optimization, conversion circuits, storage devices, and so on. Several different transduction mechanisms have been adopted for VEHs, such as electrostatic (including those which incorporate electrets), piezoelectric, electromagnetic, triboelectric, and so on. Among them, electrostatic ones are attractive for their compatibility with CMOS processes and for high power density, especially at a small scale. The ones that utilize electrets are particularly advantageous with their simple control circuit requirement (Sterken et al. 2003; Hagiwara et al. 2012).

One of the most important performance indicators of VEHs is their power harvesting capabilities, in other words, energy conversion efficiencies. In this regard, one of the crucial points in the VEH design is its frequency characteristics. In some application areas, vibration sources have well-defined peak frequencies with minimal long-term drift, which can be effortlessly matched by resonant frequencies of certain VEH designs, e.g. cantilever structures. More often than not, however, vibration sources bear broadband and stochastic spectral characteristics (termed as colored noise), and hence, it is highly imperative that VEHs be designed to match such frequency characteristics.

Various methods have been attempted so far in this context. One of the ideas has been to exploit a Duffing oscillator, i.e. an oscillator with third-order nonlinearity. While diverse realization schemes are possible, a type utilizing permanent-magnet-induced bistability has been the one that is most widely investigated (Cottone et al. 2009; Erturk et al. 2009; Sebald et al. 2011; Pereira et al. 2019; Liu et al. 2022). Another scheme is to make an array of single degree-of-freedom (DOF) structures, each of

✉ Dooyoung Hah
dooyoung.hah@agu.edu.tr

[1] Department of Electrical and Electronics Engineering, Abdullah Gül University, Erkilet Blv, 38080 Kayseri, Turkey

Published online: 05 March 2024

which has a different resonant frequency (Xue et al. 2008; Xiao et al. 2014; Lien et al. 2022). By superposing those invidual spectra, an overall broadband frequency characteristics can be realized. A similar but slightly different approach, called a multi-DOF structure, has been reported as well, where structures with different resonant frequencies are mechanically coupled together (Jang et al. 2011; Kim et al. 2011; Li et al. 2019; Saxena et al. 2021).

Yet another approach exists, which is based on nonlinear springs. This approach has a clear advantage over the aforementioned methods. Owing to its simple implementation, it is quite suitable for miniaturization, and hence, becomes quite attractive for applications with limited footprints. The simplest form of a nonlinear spring is a clamped-clamped beam, which bears a third-order nonlinearity, meeting the criteria for a Duffing oscillator (Senturia 2007). Its nonlinearity can be further enhanced by adding an initial curve to a clamped-clamped beam, which makes it a Duffing–Holmes oscillator, featuring simultaneous second- and third-order nonlinearities. Mainly two methods have been applied so far to add initial curves to clamped-clamped beams. The first method is to apply an axial load to a straight beam, inducing buckling (Van Blarigan et al. 2012; Ando et al. 2014; Eltanany et al. 2017; Osinaga et al. 2022; Wang et al. 2023). The second one is to directly design the beam in a curved shape (Ando et al. 2012; Nguyen et al. 2021; Scerri et al. 2015; Du et al. 2018), and this approach is more appropriate for applications with limited footprints because it does not require an auxiliary apparatus to exert axial load.

Recently, we also have reported on energy harvesters with this pre-shaped curved-beam hinges (Hah 2021, 2023). The main structure of the electret-based VEHs (eVEHs) of our study (Fig. 1) is based on a balanced-comb-drive configuration (Honma et al. 2018, 2019).

A mass is attached to a moving part of the comb-drive actuators from the top while electrets are formed as a dielectric layer on the sides of the comb fingers. When a mass moves in response to external vibration, engagements of comb-drive fingers change, inducing redistribution of charges in the electrets. This charge redistribution results in desired electric power generation.

A study of eVEHs with a colored-noise vibration input has not received enough attention they deserve. In our previous reports (Hah 2021, 2023), through an analytical study based on stochastic differential equations (SDEs) with colored-noise vibration as an input, we have demonstrated that eVEHs with curved-beam hinges can harvest higher electric power than the ones with ordinary straight-beam hinges for a certain range ($0.02g - 0.05g$, g: gravitational acceleration) of acceleration magnitudes. It was also reported that it is the other way around at higher ($0.1g$)

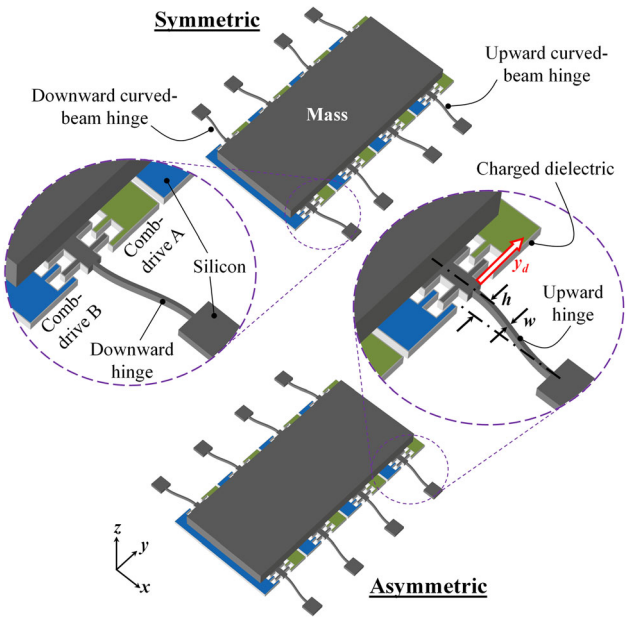

Fig. 1 Sketches of eVEHs examined in the study. (Top) symmetric and (bottom) asymmetric curved-hinge configurations

vibration magnitudes, i.e. the eVEHs with straight-beam hinges are more efficient while Roundy (2005) reported that vibration sources commonly found from our surroundings have magnitudes range from $0.01g$ to $1g$. The motivation of the current work was originated from this observation—a Duffing oscillator (with straight clamped-clamped beams) produces higher power than a Duffing–Holmes oscillator (with curved clamped-clamped beams) at high vibration magnitudes ($\geq 0.1g$).

Although the device configuration was symmetrical in almost every sense in the previous reports (Hah 2021, 2023), including the comb-drives and the loads, only the curved-beam hinges were incorporated asymmetrically; i.e. initial curves were added towards the same direction for all of the springs as illustrated in Fig. 1 (bottom). In the current study, a new configuration is proposed where a perfect symmetry is obtained by reversing the initial curves of a *half* of the hinges towards the opposite direction as depicted in Fig. 1 (top). Such a symmetric configuration cancels the second-order nonlinearity, making the device a Duffing oscillator. It is hypothesized that the new symmetric configuration (a Duffing oscillator) can produce higher power at a high vibration magnitude ($\geq 0.1g$), compared to the asymmetric configuration (a Duffing–Holmes oscillator) that was reported previously. Therefore, it is the main objective of the current work to examine the proposed eVEH with a symmetric curved-beam hinge configuration in comparison to an asymmetric one, and to prove the aforementioned hypothesis. It will be shown via numerical simulation study that the symmetrically configured eVEHs can produce higher power output than the

asymmetrical ones when the magnitude of the colored-noise vibration is higher than $0.1g$. It will be also shown that the nonlinearity of the springs can be still controlled by adjusting the curve heights of the beams.

This article is organized in the following manner. Section 2 will describe the force–displacement relationships in the symmetric configuration. Section 3 will explain the device model and the analysis method. The study results will be presented in Sect. 4.

2 Symmetric curved-beam hinge configuration

As illustrated in Fig. 1, two sets (A & B) of comb-drives are incorporated in the device in a balanced manner, each of which is connected to the corresponding load (external). Curved hinges are shaped to resemble those of the fundamental modes, i.e. a cosine function of one period. For the asymmetric-hinge eVEHs, the relationship between the restoring force ($F_{r,asym}$) and the beam-center displacement (y_d, see Fig. 1) of a curved-beam hinge can be expressed as (Casals-Terre et al. 2008):

$$F_{r,asym}(y_d) = k_1 y_d + k_2 y_d^2 + k_3 y_d^3 = F_{r,up}(y_d) \tag{1}$$

where k_1, k_2 and k_3 are a linear, a quadratic, and a cubic spring constant, respectively. This relationship holds the same for the upward curved-hinges in the symmetric configuration ($F_{r,up}$). The spring constants are dependent on the beam geometries, such as width (w), height (h, see Fig. 1), thickness (T), and length (l), as follows (Casals-Terre et al. 2008):

$$k_1 = \frac{\pi^4 EwT}{12l^3}\left(2w^2 + 3h^2\right) \tag{2}$$

$$k_2 = \frac{3\pi^4 EwTh}{8l^3} \tag{3}$$

$$k_3 = \frac{\pi^4 EwT}{8l^3} \tag{4}$$

where E is the Young's modulus of the beam. From (2)–(4), it can be understood that the beam height (h) plays a pivotal role in determining the nonlinearity of the springs, and therefore, is one of the major design parameters. For instance, it depends on the value of h whether or not a curved hinge will exhibit bistability. When h is higher than a critical beam height (h_{cr}), the beam begins to show bistability. h_{cr} is proportional to the beam width (w) in the following manner (Qiu et al. 2004):

$$h_{cr} = \frac{4\sqrt{3}}{3} w \tag{5}$$

The force–displacement relationship of the downward-curved hinges ($F_{r,dn}$) can be found by replacing F_r and y_d in (1) with $-F_r$ and $-y_d$, respectively, which becomes:

$$F_{r,dn}(y_d) = k_1 y_d - k_2 y_d^2 + k_3 y_d^3 \tag{6}$$

This makes the overall relationship in the symmetric-hinge configuration as follows:

$$F_{r,sym,total}(y_d) = \frac{N_s}{2}\left(F_{r,up} + F_{r,dn}\right) = N_s\left(k_1 y_d + k_3 y_d^3\right) \tag{7}$$

where N_s is the total number of springs. Equation (7) shows that the symmetric-hinge eVEHs becomes a Duffing oscillator, similar to the straight-hinge devices. Nevertheless, there is a clear difference between them—in case of the symmetric-hinge device, the linear spring constant (k_1) can be adjusted by varying the beam height (h) while k_3 is independent of h.

Figure 2 compares the F_r versus y_d relationships between the symmetric and the asymmetric devices for various beam heights.

The characteristics of the asymmetric devices (Fig. 2, right) show that $|F_r|$ is significantly smaller for $y_d < 0$ compared to the same magnitude of displacement for $y_d > 0$. For positive y_d, F_r rapidly increases according to y_d, but for negative y_d, F_r changes the polarity of the slope when $h > 0.5h_{cr}$. The displacement of the beam becomes more asymmetric as h increases, with movement towards negative y_d direction more favorable. A snapping behavior (for $h > 0.5h_{cr}$) and the bistability (for $h > h_{cr}$) can be also understood from the graphs of asymmetric configuration. On the other hand, the characteristics of the symmetric devices (Fig. 2, left) show a symmetry about $y_d = 0$ without snapping or bistability. From these observations, the following inference can be made. In certain conditions, asymmetric movements with a clear advantage in one direction will produce wider range of motion. In other circumstances, symmetric movements can be more beneficial because there is no specific direction that imposes high resisting force. This inference will be examined with the results in Sect. 4.

3 Device model and analysis method

The governing equation of the eVEH system can be expressed as follows:

$$m\frac{\partial^2 y_d}{\partial t^2} + c_d\frac{\partial y_d}{\partial t} + F_r(y_d) - \frac{1}{2}\frac{\partial U_e}{\partial y_d} = F_{ext} = ma_{ext} \tag{8}$$

where m is a mass attached to the moving structure (see Fig. 1), t the time, and c_d the damping coefficient. F_{ext} is the external force, caused by vibration, which is

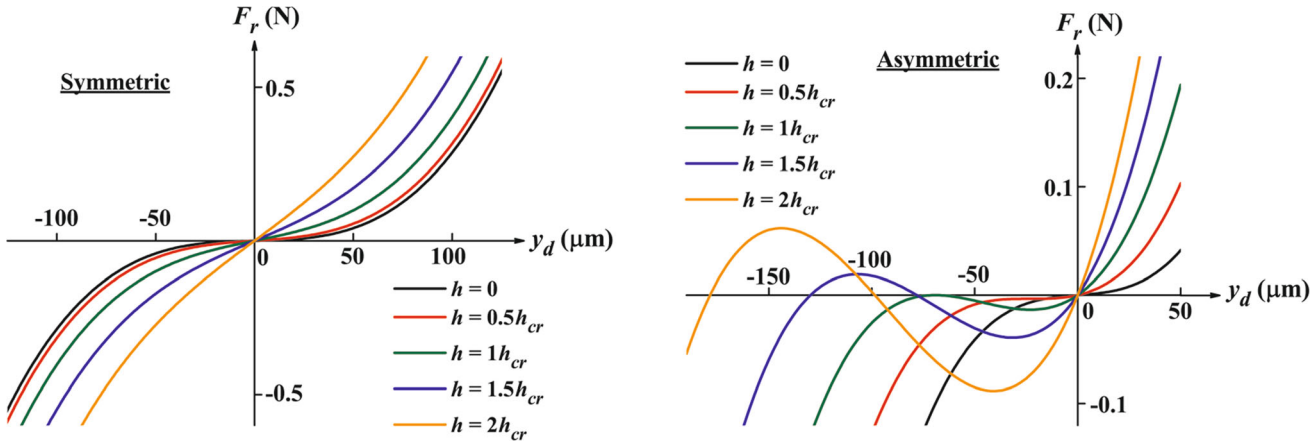

Fig. 2 Restoring force (F_r) versus beam-center displacement (y_d) of (left) symmetric and (right) asymmetric curved-beam hinge configurations for various beam heights (h). h is expressed in terms of the critical beam height (h_{cr}). For the w value of 20 μm, h_{cr} is equal to 46.2 μm

proportional to the external acceleration, a_{ext}. U_e is the electrostatic potential energy of the comb-drives A & B, which can be described as:

$$U_e = \frac{1}{2}\left[C_A(V_S - V_A)^2 + C_B(V_S - V_B)^2\right] \tag{9}$$

where V_S is the voltage associated with the initial charge on the electret, and also called surface potential. C_A and C_B are the variable capacitances of the comb-drives A & B, respectively. V_A and V_B are the voltages on the corresponding loads, R_{LA} and R_{LB}, respectively. According to the equivalent circuit model developed by Yang et al. (2019) and Hah (2023), the following equation was established with respect to the electric circuit:

$$\frac{V_i}{R_{Li}} + C_i\frac{dV_i}{dt} - (V_S - V_i)\frac{dC_i}{dt} = 0, i \in [A, B] \tag{10}$$

C_i is a function of y_d, which was calculated based on the parallel-plate capacitance formula, and adjusted by considering fringe capacitance (Hah 2023).

For the numerical analysis of the eVEHs, (8) and (10) were transformed to the following stochastic differential equations (Kloeden and Platen 1995; Ando et al. 2012; Hah 2023):

$$dy_d = y_v dt \tag{11}$$

$$dy_v = -\frac{1}{m}\left[c_d y_v + F_r(y_d) - \frac{1}{2y_v}\frac{dU_e}{dt}\right]dt + a_{ext}dt = y_a dt \tag{12}$$

$$a_{ext} = \frac{\sigma}{m}\frac{dW_t}{dt} \tag{13}$$

$$dV_i = \frac{1}{C_i}\left[(V_S - V_i)dC_i - \frac{V_i}{R_{Li}}dt\right], i \in [A, B] \tag{14}$$

dt is the time step. It was set as 50 ns for this work, which provided convergence. y_v and y_a are the beam-center velocity and the acceleration, respectively. W_t is the Wiener process that models the stochastic vibration input, and dW_t is normally distributed with a mean of zero. In this study, dW_t was generated in MATLAB® by processing a random uncorrelated time series through a low pass filter (cutoff: 500 Hz), becoming a colored noise. σ is the diffusion coefficient that sets the strength of the vibration magnitude, i.e. external acceleration (a_{ext}).

In the analysis, it was assumed that the displacement of the mass occurs only in y direction. This is a reasonable assumption because the spring constants in other directions (x or z) are several orders of magnitude higher than those in y direction. Therefore, a_{ext} implies the y component of the external acceleration. It is also assumed that the deformations of the device only occur in the curved-beam hinges. This is also reasonable because other structures can be made much wider than the hinges. In the current study, the effect of thermoviscoelasticity (Abouelregal 2022), the memory effect (Abouelregal et al. 2022), and the effect of initial stress in the beams (Abouelregal 2020) were not considered. Inclusion of these effects is considered to further enhance the understanding in the subject matter, which can be a part of the future work.

Euler–Maruyama method (Kloeden and Platen 1995) was used to solve (11)–(14), and to produce all the pertinent time series. Electric power was calculated from the voltage or current time series. Since random signals were used as the inputs, analysis was repeated many times with freshly generated Wiener process for each run. The accuracy of the results improves according to the number of repetitions. Five hundred to two thousand different time series were produced as an input for a single analysis, and the average was obtained from the resulting output time series. Figure 3 illustrates the flowchart of the simulation.

Table 1 summarizes the values of the device parameters used in the study. The materials as well as the fabrication

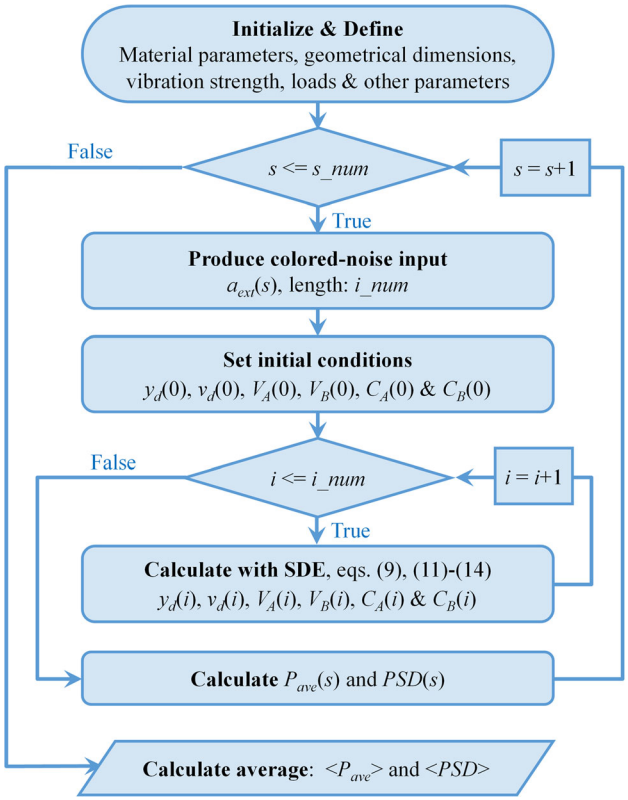

Fig. 3 Flowchart of the simulation. s_{num}, i_{num}, P_{ave} and *PSD* are the number of produced input series for repeated analysis, the length of a time series, the average power calculated for one time series, and the power spectral density of a time series, respectively. $< \cdot >$ indicates the average over simulation repetitions. *SDE* stochastic differential equation

methods assumed for the proposed devices also followed those of Honma et al. (2018, 2019). Single-crystalline silicon (SCS) was considered as the material of the main structure, which can be patterned by combination of photolithography and deep reactive ion etching (DRIE) out of a device layer of a silicon-on-insulator (SOI) substrate. The Young's modulus of 169 GPa was used for SCS in <110> direction (Hopcroft et al. 2010). The movable structures are released by selectively etching the buried oxide layer of the SOI wafer in a buffered hydrofluoric (BHF) acid. It was considered that the electrets are formed by oxidation of silicon while potassium ions are intentionally incorporated by means of a water bubbler with potassium hydroxide (KOH), which is succeeded by a polarization process (Sugiyama et al. 2012) to set the surface potential. The last step in the fabrication process is to attach a tungsten block to the movable structure to make it function as the main part of the mass. The value of c_d was derived from the results of Honma et al. (2019) as well.

4 Results and discussion

As the first step, the established model and the analysis method was tested with the experiment results of Honma et al. (2019) for verification. This was because the device structure (balanced comb-drive configuration) and most of the device parameters of the current study (Table 1) were based on those of Honma et al. (2019) as mentioned earlier in Sects. 1 and 3. In order to match the experiment conditions of Honma et al. (2019), the vibration input was set as a sinusoidal waveform with a frequency of 160 Hz and a strength of 0.65g, and the beam height (h) was set to zero. In such conditions, the output power was calculated as 1 mW by using the current simulation method, which is close to the reported value of 1.3 mW by Honma et al. (2019). Based on this comparison, it was concluded that the model and the analysis method developed in the current study was reasonable.

Then, the analysis study was continued with the colored-noise input as described in Sect. 3. Figure 4 presents examples of calculated time series (unaveraged) of various signals for both symmetric and asymmetric configurations.

Several observations can be made from Fig. 4. It is seen that for a single time series, all of the other output signals, i.e. velocity, capacitance change, and current, resemble the waveform of the displacement signal. It can be also noticed that the output signals are much smoother than the input signal (F_{ext}) due to the filtering effect of the oscillator, i.e. the energy harvester itself. At low vibration magnitude (0.02g), the output signals are comparable between the

Table 1 Device parameters and the nominal values used in the study

Description	Value	Description	Value
Mass (m)	2.5 g	Electret charging voltage (V_S)	200 V
Damping coefficient (c_d)	1 g/s	No. comb fingers (N_f)	900
No. springs (N_s)	8	Finger gap (d_0)	9 μm
Beam length (l)	8000 μm	Dielectric (electret) thickness (d_e)	0.85 μm
Beam width (w)	20 μm	Dielectric relative permittivity (ϵ_e)	3.6
Structure thickness (T)	400 μm	Initial finger overlap (l_{ol})	150 μm

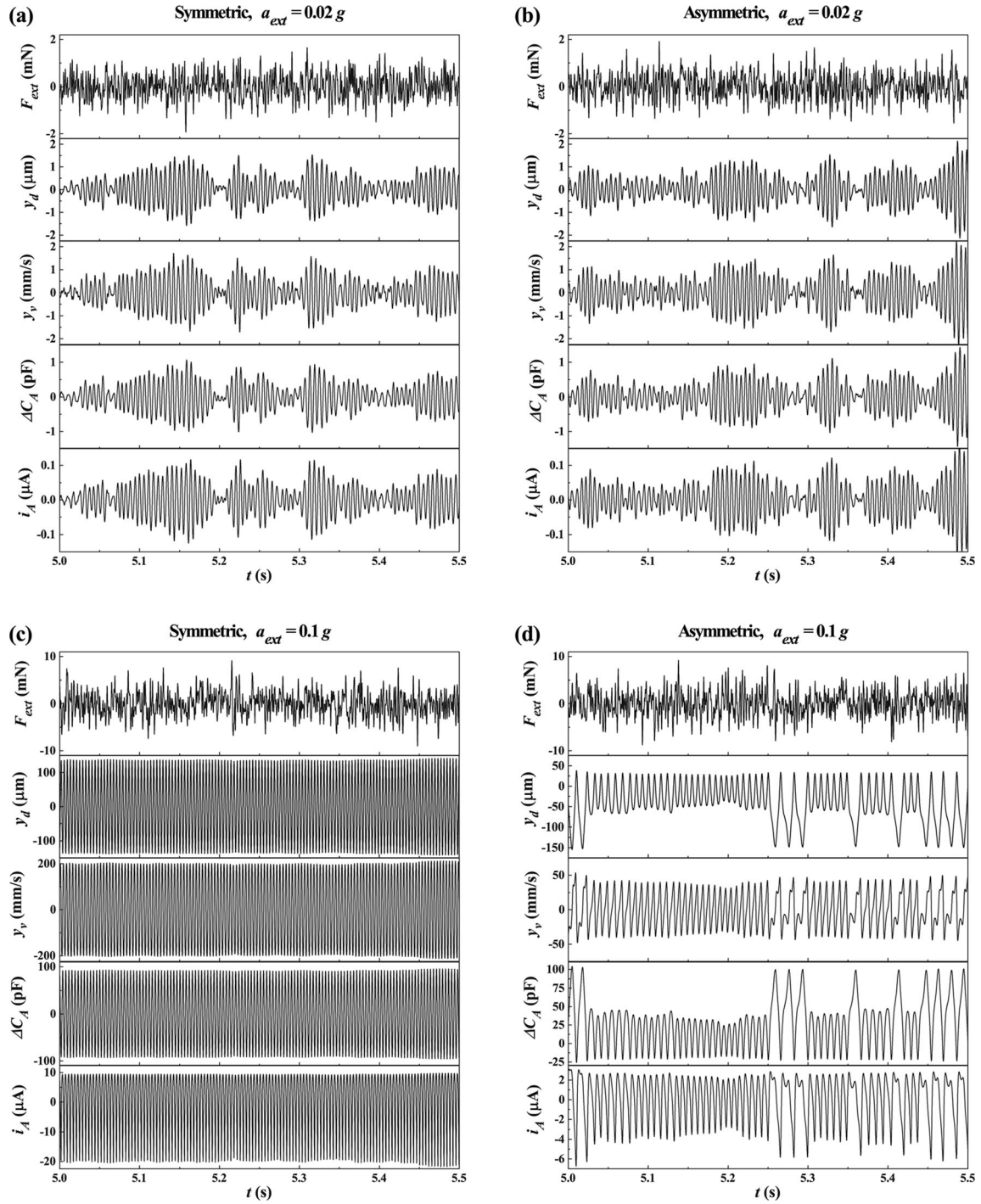

Fig. 4 Examples of signals for a duration of half a second at two different acceleration magnitudes (rms), $0.02g$ and $0.1g$. **a**, **c**: symmetric curved-beam hinge configuration. **b**, **d**: asymmetric curved-beam hinge configuration. Signals: (from top) input force ($F_{ext} = ma_{ext}$), beam-center displacement (y_d), velocity (y_v), capacitance change of comb-drive A (ΔC_A), and current through R_{LA} (i_A). Beam height $(h) = 1.5h_{cr}$

symmetric and the asymmetric configurations. At higher vibration magnitude ($0.1g$), however, they exhibit quite different behaviors from each other. While the asymmetric one shows clear inclination towards the negative direction in displacement, the symmetric one shows balanced displacement in both directions. This difference can be also observed from the phase portraits (Fig. 5c, d).

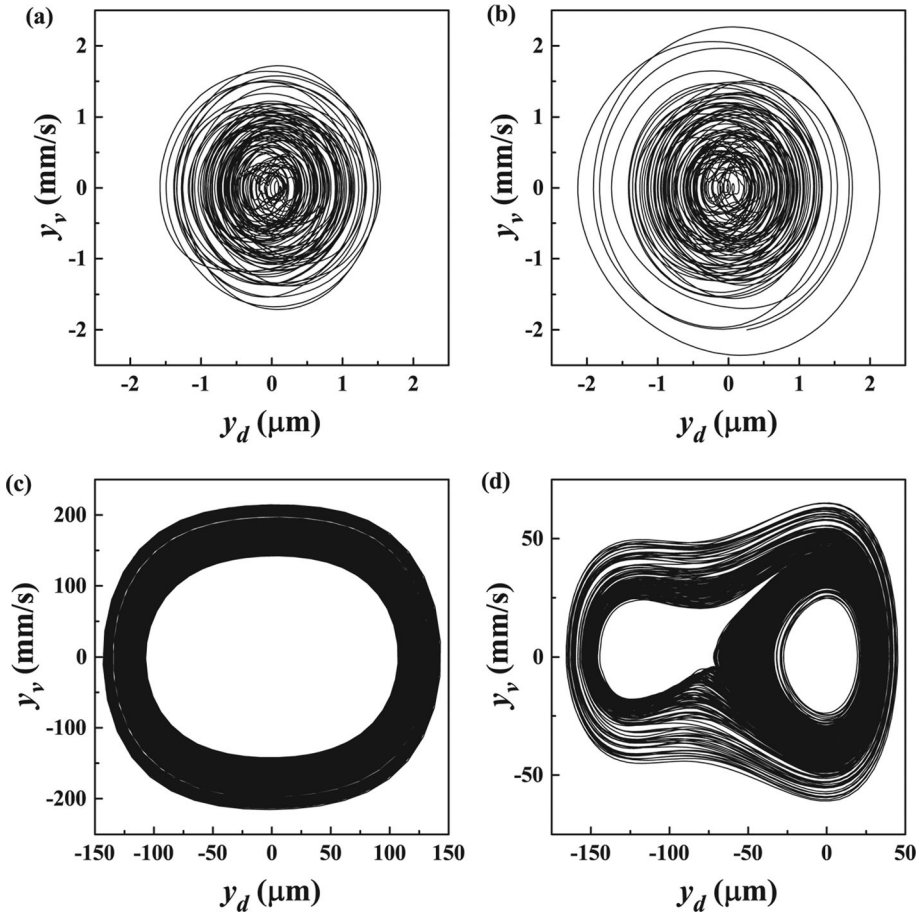

Fig. 5 Phase portraits (velocity vs. displacement) of the eVEHs with **a**, **c** symmetric and **b**, **d** asymmetric curved-beam hinge configurations for the same time range as in Fig. 4. a_{ext}: **a**, **b** $0.02g$, **c**, **d** $0.1g$. $h = 1.5h_{cr}$

It can be also seen that both configurations exhibit broad spectra at this vibration magnitude, understood from the wide trajectories instead of thin ones. Also, at this condition, the symmetric device shows higher displacements and velocities than the asymmetric one. One can also see from Fig. 4c, d that the symmetric device moves at a higher frequency than the asymmetric one in this specific condition, which agrees with the power density spectra shown later (Fig. 8). The phase portraits at $0.02g$ (Fig. 5a, b) circle around the origin, and do not show much differences between two configurations as can be seen from Fig. 4a, b.

Electric power produced by eVEHs depends on the load condition, and hence, it is sensible to compare the device performances at the optimal load condition for each case. Various parameters affect the optimal load condition, such as the device type, capacitance values, input vibration characteristics (magnitude and spectra), and so on. Figure 6 shows the effect of load resistance values to the harvested electric power, with the second parameter as the beam heights.

It can be seen that as the load resistance (R_L) increases, the optimal beam height (h_{opt}), i.e. the h value that produces the maximum power output, shifts towards a lower value, eventually becoming zero (i.e. a straight beam). It can be also understood that as the vibration magnitude increases, the optimal load resistance value decreases slightly. In the practical applications, the optimal values of the load resistance and the beam height can be determined according to the simulation results while considering the specific characteristics of the vibration source, such as strength, frequency range, randomness, and so on.

Figure 7 presents the calculated average electric power as a function of the beam heights for both types of devices at different vibration magnitudes (a_{ext}).

Only the results at the optimal load conditions for the specific a_{ext} value are included in the figure. It can be observed that in case of the symmetric devices, curved-beam hinges result in higher power outputs than the straight hinges for the range of a_{ext} values considered in the study ($0.02g-0.5g$) while the degree of enhancement becomes smaller as a_{ext} increases. The symmetrically configured devices lose the advantage when a_{ext} exceeds $0.5g$. It is also seen that the optimal beam height h_{opt} decreases as a_{ext} increases. Table 2 summarizes the highest electric power output that can be obtained at each vibration magnitude. In case of the asymmetric devices, the straight

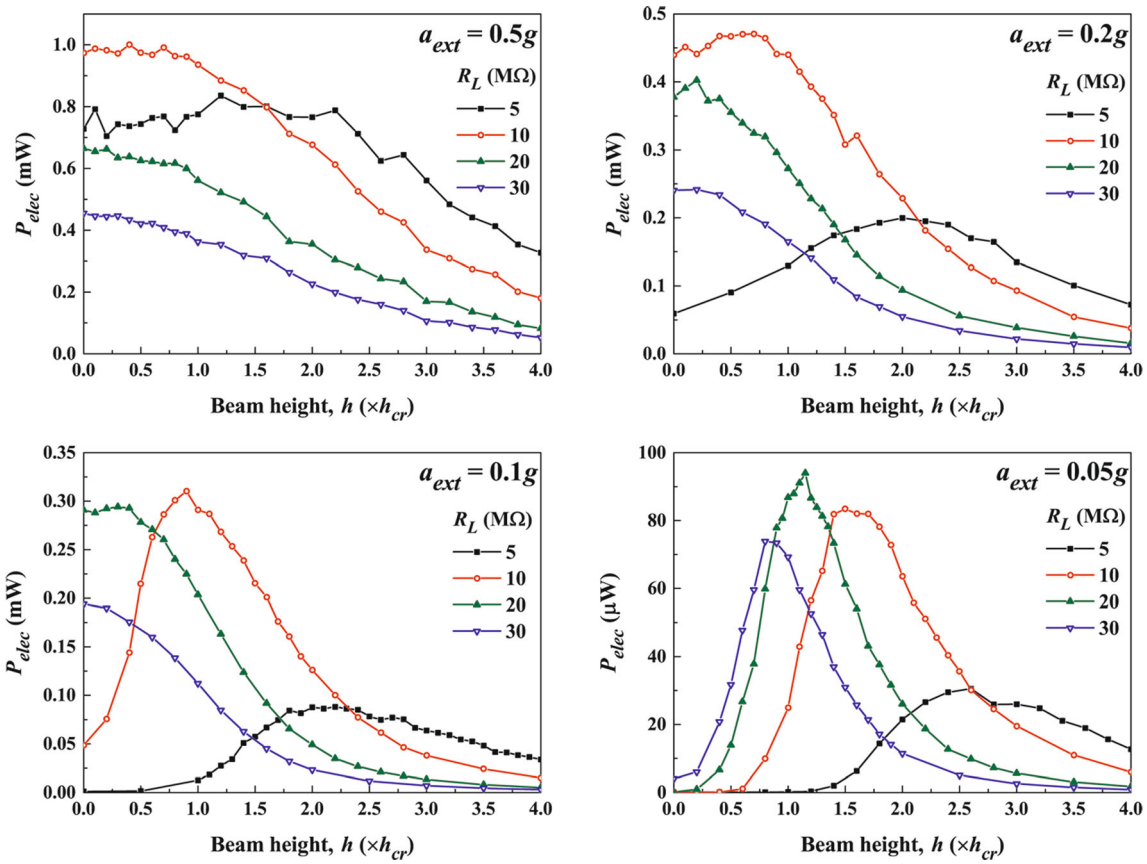

Fig. 6 Calculated average electric power (P_{elec}) of eVEHs as a function of curved-hinge beam height (h) at various loads (R_L) for the symmetric configuration. Results are presented at four different acceleration magnitudes between $0.05g$ and $0.5g$

hinge devices were more efficient than the curved hinge ones for $a_{ext} \geq 0.1g$. It can be concluded that the devices with the symmetric hinge configuration can produce higher power (as much as 7.3% more) than the asymmetric configuration for the vibration magnitude range of $0.1g$–$0.5g$. When compared to the straight-hinge device, the symmetric device can produce as much as 4.5 times higher power, maximum improvement occurring at $0.05g$. It was also learned that the optimal load values decrease as a_{ext} increases.

Examples of the power spectral density (PSD) graphs are presented in Fig. 8 for both types of the devices at optimum load conditions. At a low vibration magnitude ($0.02g$), most of the spectra show those of typical linear harmonic oscillators, implying that the nonlinearity is rather weak at this magnitude. In case of symmetric devices, spectral peaks always shift towards the higher frequency as the beam height increases regardless of vibration magnitudes. For $h = 0$ in a symmetric device and for $h = h_{cr}$ in an asymmetric device, nonlinear and broadband features are apparent. At higher vibration magnitude ($0.1g$), spectra become much broader and nonlinear characteristics are more clearly shown for the low beam heights (h: $0-2h_{cr}$). For this range of h, spectra of asymmetric devices tend to shift towards the lower frequency as h increases. For the symmetric device, although the spectrum is broader when h is 0, PSD is much higher around the peak when h is $1h_{cr}$. At $0.5g$ of vibration magnitude, spectra become substantially broader. The spectra of asymmetric devices do not change significantly for different beam heights. Differences among spectra of different beam heights are still unambiguous for the symmetric devices.

5 Conclusion

In this study, a symmetric configuration of curved-beam hinges was proposed for eVEHs. Via numerical simulation based on stochastic differential equations, power harvesting performances of the proposed eVEHs were estimated for a range ($0.02g-0.5g$) of colored-noise vibration magnitudes. It was learned that symmetrically configured

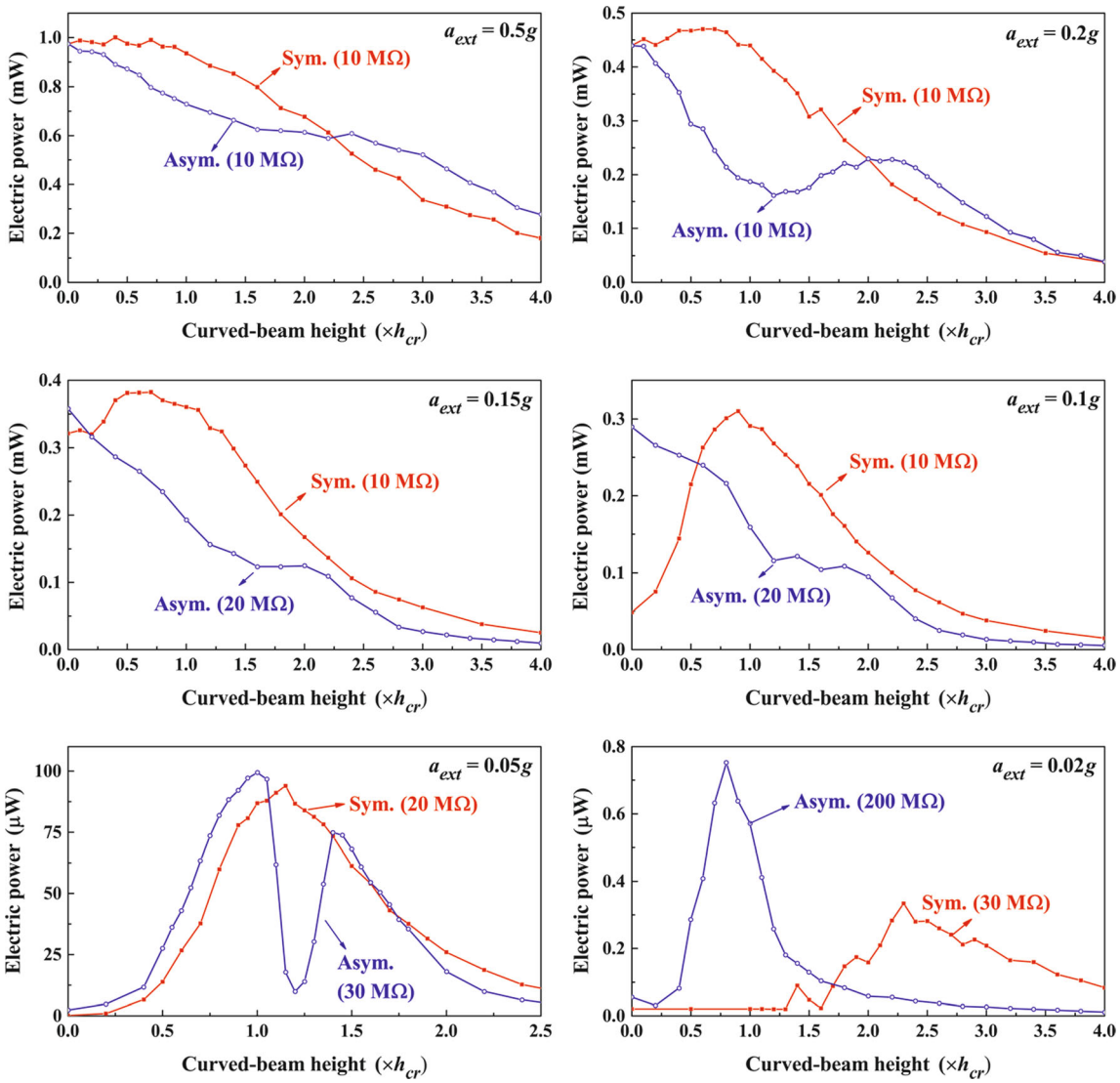

Fig. 7 Calculated average electric power (P_{elec}) of eVEHs as a function of curved-hinge beam height (h) at various acceleration magnitudes (a_{ext}) for both configurations. The optimal load conditions are written next to the curves

Table 2 Comparison of maximum electric power outputs between the symmetric and the asymmetric configurations

	Symmetric		Asymmetric		Straight
a_{ext} (g)	P_{elec} (μW)	h_{opt} (h_{cr})	P_{elec} (μW)	h_{opt} (h_{cr})	P_{elec} (μW)
0.02	0.334	2.3	0.752	0.8	0.250
0.05	94.0	1.2	99.4	1.0	20.8
0.10	310	0.9	289	0.0	289
0.15	383	0.7	358	0.0	358
0.20	470	0.7	439	0.0	439
0.50	1001	0.4	974	0.0	974

The best power outputs of the straight-hinge device ($h = 0$) are also included

devices can produce higher power output than the asymmetrical ones for high vibration magnitudes ($a_{ext} \geq 0.1g$). It should be noted that the results reported here are for the specific input conditions provided. The results may differ if the input vibration characteristics change, e.g. if it is not colored noise, if its spectrum is different from the one used, etc. In this work, the model and the analysis was applied to a specific type of devices, i.e. eVEHs. It can be further extended to other types of VEHs with proper modelling of the transduction mechanisms, such as piezoelectric, electromagnetic, etc, which will be a part of the future works.

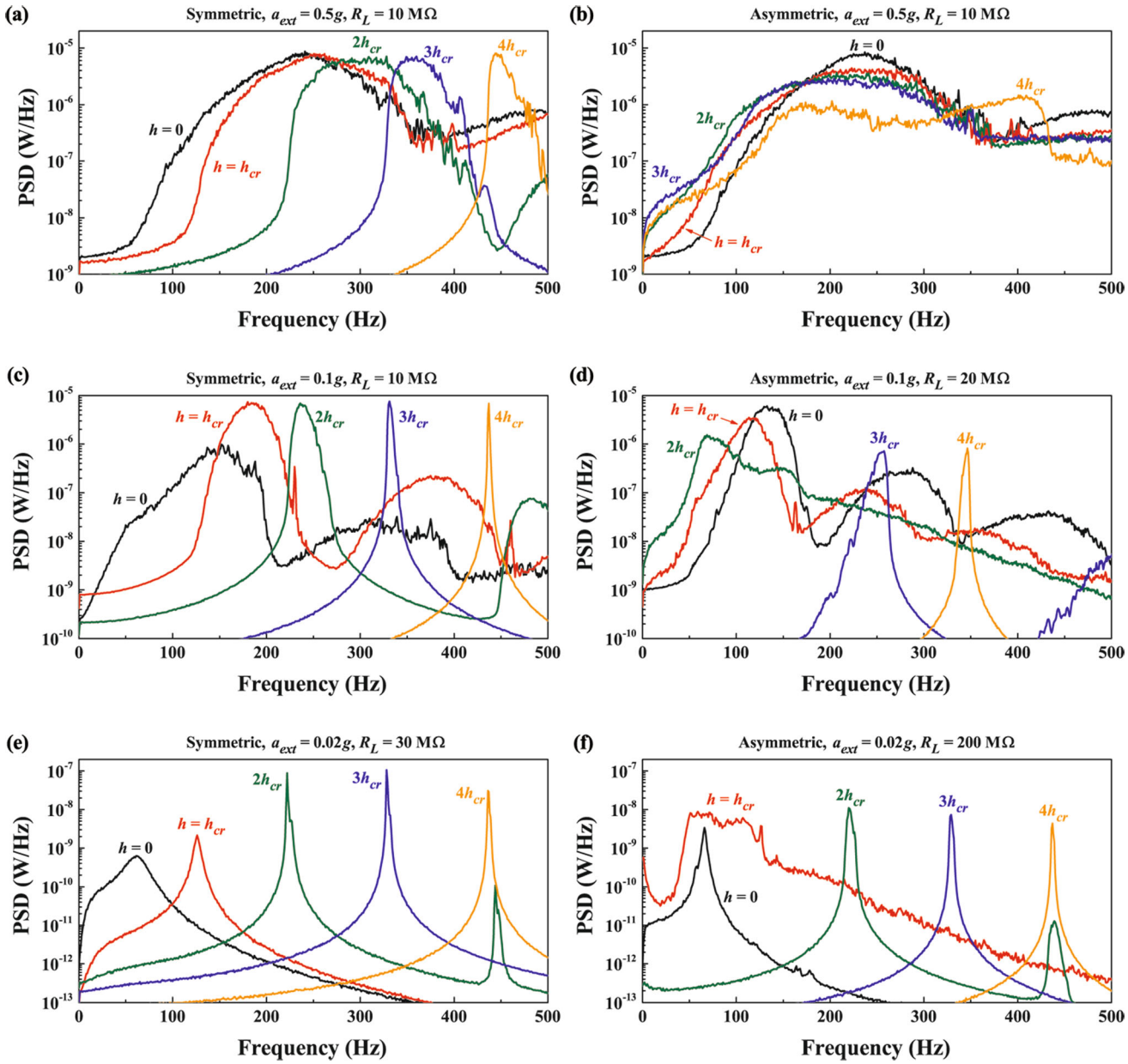

Fig. 8 Electric power spectral density (PSD) of eVEHs for both configurations at optimal load conditions. a_{ext}: **a**, **b** 0.5g, **c**, **d** 0.1g, and **e**, **f** 0.02g. **a**, **c**, and **e**: symmetric, **b**, **d**, and **f**: asymmetric configuration

Data availability Data sets generated during the current study are available from the corresponding author on reasonable request.

Declarations

Conflict of interest The author has no competing interests to declare that are relevant to the content of this article.

References

Abouelregal AE (2020) Size-dependent thermoelastic initially stressed micro-beam due to a varying temperature in the light of the modified couple stress theory. Appl Math Mech 41:1805–1820. https://doi.org/10.1007/s10483-020-2676-5

Abouelregal AE (2022) Modeling and analysis of a thermoviscoelastic rotating micro-scale beam under pulsed laser heat supply using multiple models of thermoelasticity. Thin-Walled Struct 174(109):150. https://doi.org/10.1016/j.tws.2022.109150

Abouelregal AE, Mohammed FA, Benhamed M et al (2022) Vibrations of axially excited rotating micro-beams heated by a high-intensity laser in light of a thermo-elastic model including the memory-dependent derivative. Math Comput Simul 199:81–99. https://doi.org/10.1016/j.matcom.2022.03.017

Ando B, Baglio S, L'Episcopo G et al (2012) Investigation on mechanically bistable mems devices for energy harvesting from vibrations. J Microelectromech Syst 21(4):779–790. https://doi.org/10.1109/JMEMS.2012.2192912

Ando B, Baglio S, Bulsara A et al (2014) A bistable buckled beam based approach for vibrational energy harvesting. Sens Actuators A 211:153–161. https://doi.org/10.1016/j.sna.2013.12.027

Casals-Terre J, Fargas-Marques A, Shkel AM (2008) Snap-action bistable micromechanisms actuated by nonlinear resonance. J Microelectromech Syst 17(5):1082–1093. https://doi.org/10.1109/JMEMS.2008.2003054

Cottone F, Vocca H, Gammaitoni L (2009) Nonlinear energy harvesting. Phys Rev Lett 102(080):601. https://doi.org/10.1103/PhysRevLett.102.080601

Du H, Chau FS, Zhou G (2018) Harmonically-driven snapping of a micromachined bistable mechanism with ultra-small actuation stroke. J Microelectromech Syst 27(1):34–39. https://doi.org/10.1109/JMEMS.2017.2785331

Eltanany AM, Yoshimura T, Fujimura N et al (2017) Development of piezoelectric bistable energy harvester based on buckled beam with axially constrained end condition for human motion. Jpn J Appl Phys 56(10S):10PD02. https://doi.org/10.7567/JJAP.56.10PD02

Erturk A, Hoffmann J, Inman DJ (2009) A piezomagnetoelastic structure for broadband vibration energy harvesting. Appl Phys Lett 94(25):254102. https://doi.org/10.1063/1.3159815

Hagiwara K, Goto M, Iguchi Y et al (2012) Electret charging method based on soft x-ray photoionization for mems transducers. IEEE Trans Dielectr Electr Insul 19(4):1291–1298. https://doi.org/10.1109/TDEI.2012.6260003

Hah D (2021) Effects of curved-beam heights to harvested energy in a balanced comb-drive configuration. In: 2021 Symposium on design, test, integration & packaging of MEMS and MOEMS (DTIP). https://doi.org/10.1109/DTIP54218.2021.9568673

Hah D (2023) Analysis of electret-based vibration energy harvesting devices with curved-beam hinges. J Intell Mater Syst Struct 34(14):1702–1712. https://doi.org/10.1177/1045389X231151249

Honma H, Mitsuya H, Hashiguchi G et al (2018) Improvement of energy conversion effectiveness and maximum output power of electrostatic induction-type mems energy harvesters by using symmetric comb-electrode structures. J Micromech Microeng 28(6):064005. https://doi.org/10.1088/1361-6439/aab514

Honma H, Tohyama Y, Toshiyoshi H (2019) A 1.3 milliwatts electrostatic vibrational energy harvester with minimal reactive power through reduced internal stray capacitances. In: 2019 20th international conference on solid-state sensors, actuators and microsystems & eurosensors XXXIII (TRANSDUCERS & EUROSENSORS XXXIII). https://doi.org/10.1109/TRANSDUCERS.2019.8808249

Hopcroft MA, Nix WD, Kenny TW (2010) What is the Young's modulus of silicon? J Microelectromech Syst 19(2):229–238. https://doi.org/10.1109/JMEMS.2009.2039697

Jang SJ, Rustighi E, Brennan MJ et al (2011) Design of a 2D of vibrational energy harvesting device. J Intell Mater Syst Struct 22(5):443–448. https://doi.org/10.1177/1045389X10393766

Kim IH, Jung HJ, Lee BM et al (2011) Broadband energy harvesting using a two degree-of-freedom vibrating body. Appl Phys Lett 98(214):102. https://doi.org/10.1063/1.3595278

Kloeden P, Platen E (1995) Numerical solution of stochastic differential equations. Springer, New York

Li X, Yu K, Upadrashta D et al (2019) Multi-branch sandwich piezoelectric energy harvester: mathematical modeling and validation. Smart Mater Struct 28(3):035010. https://doi.org/10.1088/1361-665X/aaf8bf

Lien IC, Lo YC, Chiu SH et al (2022) Comparison between overall and respective electrical rectifications in array of piezoelectric energy harvesting. J Mech 38:518–530. https://doi.org/10.1093/jom/ufac039

Liu H, Zhao L, Chang Y et al (2022) Parameter optimization of magnetostrictive bistable vibration harvester with displacement amplifier. Int J Mech Sci 223(107):291. https://doi.org/10.1016/j.ijmecsci.2022.107291

Nguyen SD, Halvorsen E, Paprotny I (2021) Bistable springs for wideband microelectromechanical energy harvesters. Appl Phys Lett 102(2):023904. https://doi.org/10.1063/1.4775687

Osinaga SM, Machado SP, Febbo M (2022) An analytical model of the electromechanical coupling for a piezoelectric stepped buckled beam for energy harvesting applications. Mech Syst Signal Process 179(109):355. https://doi.org/10.1016/j.ymssp.2022.109355

Pereira TL, de Paula AS, Fabro AT et al (2019) Random effects in a nonlinear vibration-based piezoelectric energy harvesting system. Int J Bifurc Chaos 29(4):1950046. https://doi.org/10.1142/S0218127419500469

Qiu J, Lang JH, Slocum AH (2004) A curved-beam bistable mechanism. J Microelectromech Syst 13(2):137–146. https://doi.org/10.1109/JMEMS.2004.825308

Roundy S (2005) On the effectiveness of vibration-based energy harvesting. J Intell Mater Syst Struct 16:809–823. https://doi.org/10.1177/1045389X05054042

Saxena S, Dwivedi RK, Khare V (2021) Effects of cavity in a multi-resonant piezoelectric energy harvester with one straight and two l-shaped branches. Appl Phys A 127:798. https://doi.org/10.1007/s00339-021-04928-5

Scerri J, Grech I, Gatt E et al (2015) Reduced-order model for mems PZT vibrational energy harvester exhibiting buckling bistability. Electron Lett 51(5):409–411. https://doi.org/10.1049/el.2014.3804

Sebald G, Kuwano H, Guyomar D et al (2011) Experimental duffing oscillator for broadband piezoelectric energy harvesting. Smart Mater Struct 20(10):102001. https://doi.org/10.1088/0964-1726/20/10/102001

Senturia SD (2007) Microsystem design. Springer, New York

Sterken T, Baert K, Puers R et al (2003) A new power mems component with variable capacitance. In: Mircoelectronics symposium and exhibition

Sugiyama T, Aoyama M, Shibata Y et al (2012) SiO2 electret induced by potassium ions on a comb-drive actuator. In: 2012 IEEE 25th international conference on micro electro mechanical systems (MEMS)

Van Blarigan L, Danzl P, Moehlis J (2012) A broadband vibrational energy harvester. Appl Phys Lett 100(25):253904. https://doi.org/10.1063/1.4729875

Wang X, Du Q, Zhang Y et al (2023) Dynamic characteristics of axial load bi-stable energy harvester with piezoelectric polyvinylidene fluoride film. Mech Syst Signal Process 188(110):065. https://doi.org/10.1016/j.ymssp.2022.110065

Xiao Z, Yang TQ, Dong Y et al (2014) Energy harvester array using piezoelectric circular diaphragm for broadband vibration. Appl Phys Lett 104(22):223904. https://doi.org/10.1063/1.4878537

Xue H, Hu Y, Wang QM (2008) Broadband piezoelectric energy harvesting devices using multiple bimorphs with different operating frequencies. IEEE Trans Ultrason Ferroelectr Freq Control 55(9):2104–2108. https://doi.org/10.1109/TUFFC.903

Yang Z, Tang L, Tao K et al (2019) Modelling and validation of electret-based vibration energy harvesters in view of charge migration. Int J Precis Eng Manuf-Green Technol 8:113–123. https://doi.org/10.1007/s40684-019-00156-8